

# Space-time monitoring of seafloor velocity changes using seismic ambient noise

Peng Guo<sup>1,2</sup>, Erdinc Saygin<sup>1,2</sup> and Brian Kennett<sup>3</sup>

<sup>1</sup>Deep Earth Imaging Future Science Platform, The Commonwealth Scientific and Industrial Research Organisation (CSIRO), Kensington, Western Australia 6151, Australia

<sup>2</sup>Energy, The Commonwealth Scientific and Industrial Research Organisation (CSIRO), Kensington, Western Australia 6151, Australia

<sup>3</sup>Research School of Earth Sciences, The Australian National University, Canberra, Australian Capital Territory 2601, Australia

## Key Points:

- We present a new method for space-time monitoring of subsurface velocity changes in the horizontal and depth domain using seismic ambient noise.
- We compute time-lapse images of seafloor seismic velocity and observe shear-wave velocity changes up to 0.8%.
- The method opens new avenues for 4-D subsurface monitoring using dense passive seismic arrays.

---

Corresponding author: Peng Guo, [peng.guo@csiro.au](mailto:peng.guo@csiro.au); [pengguo.geos@gmail.com](mailto:pengguo.geos@gmail.com)

**Abstract**

We use seismic ambient noise recorded by dense ocean bottom nodes (OBNs) in the Gorgon gas field, Western Australia, to compute time-lapse seafloor models of shear-wave velocity. The extracted hourly cross-correlation (CC) functions in the frequency band 0.1 – 1 Hz contain mainly Scholte waves with very high signal to noise ratio. We observe temporal velocity variations ( $dv/v$ ) at the order of 0.1% with a peak velocity change of 0.8% averaged from all station pairs, from the conventional time-lapse analysis with the assumption of a spatially homogeneous  $dv/v$ . With a high-resolution reference (baseline) model from full waveform inversion of Scholte waves, we present an elastic wave equation based double-difference inversion (EW-DD) method, using arrival time differences between the reference and time-lapsed Scholte waves, for mapping temporally varying  $dv/v$  in the heterogeneous subsurface. The time-lapse velocity models reveal increasing/decreasing patterns of shear-wave velocity in agreement with those from the conventional analysis. The velocity variation exhibits a  $\sim 24$ -hour cycling pattern, which appears to be inversely correlated with sea level height, possibly associated with dilatant effects for porous, low-velocity shallow seafloor and rising pore pressure with higher sea level. This study demonstrates the feasibility of using dense passive seismic surveys for quantitative monitoring of subsurface property changes in the horizontal and depth domain.

**Plain Language Summary**

Unlike seismic waves generated by earthquakes or human-made sources, seismic ambient noise is the ubiquitous background vibration of the solid Earth recorded by seismic sensors, mainly due to the interaction of ocean waves and the seafloor. We extract virtual Scholte waves travelling along the interface between the ocean and the seafloor, using seismic interferometry on an hourly basis, from the seafloor ambient noise recorded by dense ocean bottom nodes. Conventional passive monitoring techniques assume a spatially homogeneous relative velocity changes. With this assumption, the waveform differences on the extracted Scholte waves reveal temporal variations in the velocity of shear waves up to 0.8%. The velocity variation in this study exhibits a  $\sim 24$ -hour cycling pattern, which seems inversely correlated with sea level height, possibly associated with dilatant effects for porous, low-velocity shallow seafloor and rising pore pressure with high sea level. Furthermore, we push the limits of passive monitoring with advanced wave-equation based inversion technique enabling mapping the velocity change into detailed spatial distribution. Therefore we not only infer how velocity changes in time but also provide insights on where the velocity changes occur in 3-D beneath the seabed.

**1 Introduction**

Seismic ambient noise (passive seismic data) is an ubiquitous background vibration of the solid Earth recorded by seismic sensors (Longuet-Higgins, 1950; Nishida, 2013; Arduin et al., 2015). The primary sources of seismic ambient noise are loads on the Earth's surface from pressure perturbations in the ocean and the atmosphere (Stehly et al., 2006; Gualtieri et al., 2020). Besides the low-frequency Earth's hum with periods longer than 30 s (Arduin et al., 2015), seismic ambient noise contains mainly primary (10 - 20 s) and secondary (5 - 10 s) microseisms. The primary mechanism comes from the direct coupling between the ocean waves and the solid Earth, with a period similar to that of the main ocean swell (Hasselmann, 1963). The secondary mechanism comes from the non-linear interaction between direct swells and those reflected at the coast (Longuet-Higgins, 1950; Lindsey et al., 2019). A cross-correlation (CC) of the ambient noise wavefield recorded at two receivers provides an estimate of the empirical interstation Green's function, which can be interpreted as the seismic response that would be measured at one of the receiver locations as if there is a source at the other location (Campillo & Paul, 2003; Shapiro & Campillo, 2004; Roux et al., 2005; Larose et al., 2006; Bensen et al., 2007; Saygin &

67 Kennett, 2012; Nakata et al., 2016). The dominant signals extracted from seismic am-  
 68 bient noise are usually surface waves (e.g. Shapiro & Campillo, 2004; Stehly et al., 2006;  
 69 Brenguier et al., 2016; Chen & Saygin, 2022), though body waves have also been observed  
 70 in favourable circumstances (e.g. Roux et al., 2005; Nakata et al., 2016; Saygin et al.,  
 71 2017; Castellanos et al., 2020).

72 Temporal variations of subsurface physical properties have been often observed; for  
 73 example, from environmental changes (Sens-Schönfelder & Wegler, 2006; Takano et al.,  
 74 2014, 2019; Hillers et al., 2015; Clements & Denolle, 2018; Mao et al., 2022; Kramer et  
 75 al., 2023; S. Zhang et al., 2023) and within zones of active tectonic activities such as vol-  
 76 canos and faults (Poupinet et al., 1984; Wegler et al., 2006; Brenguier et al., 2008; Mi-  
 77 nato et al., 2012; Brenguier et al., 2016; Viens et al., 2018; Barreyre et al., 2022; Tone-  
 78 gawa et al., 2023), natural resources (e.g., hydrocarbon, geothermal) production fields  
 79 (Batzle & Wang, 1992; Lumley, 2001; Obermann et al., 2015; Sánchez-Pastor et al., 2019),  
 80 and carbon/hydrogen underground storage in subsurface rock formations (Arts et al.,  
 81 2004; Lumley, 2010; Zhu et al., 2019; Ringrose et al., 2021; Krevor et al., 2023). The re-  
 82 lative change in the speed of seismic waves ( $dv/v$ ) has been widely used as a proxy for  
 83 the changes of in-situ subsurface rock physical properties. In recent years it has been demon-  
 84 strated that subsurface monitoring using seismic ambient noise is a powerful and cost-  
 85 effective solution for detecting and quantifying the time-lapse  $dv/v$  (Sens-Schönfelder &  
 86 Wegler, 2006; Brenguier et al., 2014; Hillers et al., 2015; Obermann et al., 2015; Clements  
 87 & Denolle, 2018; Sánchez-Pastor et al., 2019; Takano et al., 2019; Brenguier et al., 2020;  
 88 Mao et al., 2022; Tonegawa et al., 2023). The ever-present natural ambient sources en-  
 89 able continuous and reliable estimates of interstation seismic responses for pairs of seis-  
 90 mic stations across time, for example at a daily (Hadziioannou et al., 2011; Minato et  
 91 al., 2012; de Ridder & Biondi, 2013; Brenguier et al., 2020) or hourly basis (Mao et al.,  
 92 2019; Oakley et al., 2021; Kramer et al., 2023; Takano & Nishida, 2023). The waveform  
 93 changes (e.g., the travel time shifts) between the reference and time-lapse CC functions  
 94 can be used for estimating  $dv/v$  (Sens-Schönfelder & Wegler, 2006; Clarke et al., 2011;  
 95 Richter et al., 2014; Lecocq et al., 2014). Compared with expensive controlled-source seis-  
 96 mic surveys for time-lapse monitoring (Lumley, 2001; Hicks et al., 2016), seismic mon-  
 97 itoring using ambient noise helps reduce the operational cost significantly, is environmen-  
 98 tally friendly and can be more readily embraced by the community. Passive monitoring  
 99 is also preferred over subsurface monitoring methods that rely on naturally occurred earth-  
 100 quakes, because the latter lacks repeatability and universal distribution (Kamei & Lum-  
 101 ley, 2017).

102 The extracted empirical interstation seismic responses contain the direct (ballistic)  
 103 and multi-scattered coda waves. Both have been used for monitoring temporal variabil-  
 104 ity of subsurface velocities (Snieder et al., 2002; Sens-Schönfelder & Wegler, 2006; Takano  
 105 et al., 2020; Fokker et al., 2023). It is common practice for seismic passive monitoring  
 106 to detect the temporal changes with an assumption of spatially homogeneous change (Snieder  
 107 et al., 2002; Sens-Schönfelder & Wegler, 2006). However, it remains challenging to map  
 108 or localize the detailed spatial distribution. There have been studies using direct arrivals  
 109 of surface waves (de Ridder & Biondi, 2013; de Ridder et al., 2014; Mordret et al., 2014)  
 110 that localize the velocity changes in the horizontal plane, and use the eikonal equation  
 111 to describe the physics, which is less accurate than inversion methods based on the full  
 112 elastic-wave equations. Mordret et al. (2020) estimated velocity velocity changes in depth  
 113 from dispersion measurements using a 1-D assumption. For multiply scattered coda waves,  
 114 the spatial extent of the velocity changes can be determined from travel-time shifts us-  
 115 ing the coda-wave sensitivity kernels, which describe wave propagation by delineating  
 116 the likelihood of travel path in a statistically characterized scattering media (Pacheco  
 117 & Snieder, 2005; Obermann, Planès, et al., 2013; Obermann, Schimmel, et al., 2013; Marg-  
 118 erin et al., 2016; Sánchez-Pastor et al., 2018; Rodríguez Tribaldos & Ajo-Franklin, 2021;  
 119 Mao et al., 2022, 2023). Coda waves allow the detection of subtle velocity changes on  
 120 the order of 0.01% (Sens-Schönfelder & Wegler, 2006; Mao et al., 2019), but the spatial

121 resolution is relatively low. Compared with the established workflows for determining  
 122 quantitative 4-D (space-time) models of temporal velocity changes using body waves from  
 123 controlled seismic sources (e.g. Lumley, 2001, 2010; Z. Zhang & Huang, 2013; Yang et  
 124 al., 2016; Hicks et al., 2016; Ringrose et al., 2021), there has been a significant knowl-  
 125 edge gap for subsurface space-time monitoring using surface waves from ambient noise.

126 We present a pilot study for space-time monitoring of subsurface physical property  
 127 changes using ocean bottom ambient noise data, which not only enables the detection  
 128 of temporal average changes but also provides insights into their spatial distribution. We  
 129 extract Scholte waves in the frequency band 0.1 – 1 Hz on an hourly basis from two-day  
 130 seafloor seismic noise recorded by a dense array of ocean bottom nodes (OBNs). Time-  
 131 lapse analysis shows temporal changes of the seafloor velocity up to  $\sim 0.8\%$ . With a seafloor  
 132 model from full waveform inversion (FWI) of reference Scholte waves, we propose an elastic  
 133 wave equation based double-difference inversion (EW-DD) method using differential  
 134 wave arrival times for mapping time-lapse velocity changes in space. Synthetic and field  
 135 data applications show that it is feasible to perform space-time subsurface monitoring  
 136 using ambient noise, i.e., detecting and localizing subtle subsurface velocity changes us-  
 137 ing ambient noise data from dense seismic arrays.

## 138 2 Data and Ambient Noise Interferometry

139 Between November 2015 and April 2016, Chevron Australia and its partners ac-  
 140 quired a three-dimensional (3-D) seismic survey using active-source ocean bottom nodes  
 141 (OBNs) over the Gorgon gas field for a better description of the Gorgon reservoir sands  
 142 for carbon capture and storage. The survey area is located on the North West Shelf off-  
 143 shore of Western Australia, approximately 200 km from the mainland (Figure 1a and  
 144 1b). Both the in-line and cross-line intervals were 375 m, with 120 OBN lines covering  
 145 an area of  $\sim 436$  km<sup>2</sup>. The inline direction was  $115^\circ/295^\circ$ , about perpendicular to the  
 146 coastal line. The water depth in the survey region was between 200 and 600 m. The sur-  
 147 vey contains 3099 seismic nodes, which were deployed from the north to the south and  
 148 gradually covered the whole area of the Gorgon field with a rolling phase deployment  
 149 (Chen & Saygin, 2022). At the peak of the survey, over 1,000 nodes were recording si-  
 150 multaneously. Each node comprised four channels, with two horizontal components (X,  
 151 Y) and one vertical component (Z) for measuring displacement, and a hydrophone com-  
 152 ponent for recording pressure. The data were recorded continuously with a 2 millise-  
 153 cond interval. The survey used controlled air-gun seismic sources, but there were several  
 154 quiet time windows without using controlled active sources, for example, during public  
 155 holidays. Clock drift has been corrected during data preprocessing (Rentsch et al., 2023).  
 156 The recorded ambient seismic wavefield in the absence of active seismic sources provides  
 157 the opportunity for passive subsurface monitoring using a dense seismic array of indus-  
 158 trial scale. We select a time window around the New Year’s holiday, Julian Days 1 and  
 159 2 of 2016, for the passive seismic monitoring experiment.

160 We detrend and down-sample the vertical component of the data from 250 Hz to  
 161 20 Hz with anti-aliasing filtering. The ambient noise data are then filtered to the frequency  
 162 band 0.1 – 1 Hz. We divide the recordings of the selected quiet time window without ac-  
 163 tive source shooting into hour-long segments; each segment is then subdivided into 45  
 164 s long records with a 50% overlap. We calculate CC functions for each time window of  
 165 ambient noise recordings for all the station pairs, and use the phase-weighted stacking  
 166 (Schimmel et al., 2011) within each hour-long segment to improve the signal to noise ra-  
 167 tio. Figure 1c shows the CC functions at Hour 15 Day 1 for Line 3924 (in-line direction,  
 168 indicated by the black arrow in Figure 1b), which contain mainly Scholte waves (trav-  
 169 elling along the interface between the ocean and the seafloor) and provide constraints  
 170 on the shear-wave velocity of the seafloor. This is consistent with the observation that  
 171 interface waves, for example Rayleigh waves for the air-solid interface or Scholte waves  
 172 for the fluid-solid interface, dominate the vertical component of the microseism records

173 (Gualtieri et al., 2020). The extracted hourly CC functions have a very high signal to  
 174 noise ratio. The energy concentrates on the positive side of the CC time lags and the  
 175 empirical Scholte waves are barely visible in the acausal side, suggesting that most of  
 176 the ambient noise between 0.1 and 1 Hz propagates from the coast to the ocean in this  
 177 particular scenario.

### 178 **3 Methods and results**

#### 179 **3.1 Temporal monitoring of seismic velocity**

180 For each station pair, reference (baseline) data can be obtained by stacking the repet-  
 181 itive estimates of CC functions for that pair across all the available hours from the two-  
 182 day passive noise data recordings. We compare the causal part of the direct Scholte wave  
 183 arrivals of the reference data with that of the hourly CC functions (monitoring data) to  
 184 quantify the velocity variations in time ( $dv/v$ ). We apply Moving-Window Cross-Spectral  
 185 Analysis (Poupinet et al., 1984; Clarke et al., 2011) to the Scholte waves, with the as-  
 186 sumption that  $dv/v$  is homogeneous in space. Figures 2a and 2b depict the derived ve-  
 187 locity changes from two selected station pairs. Figure 2c shows the velocity changes from  
 188 all the station pairs, along with the corresponding average changes across the entire two-  
 189 day monitoring period. We observe seafloor velocity changes up to 0.8% (Figure 2c), ex-  
 190 hibiting a probable sinusoidal pattern with a cycle close to 24 hours. The velocity changes  
 191 in Figure 2 can be interpreted as the average velocity perturbation of the subsurface medium  
 192 through which the Scholte waves propagate. The temporal changes of velocities from more  
 193 survey lines, as indicated by the black arrows in Figure S1, are shown in Figure S2, sug-  
 194 gesting similar patterns of velocity changes in line with Figure 2.

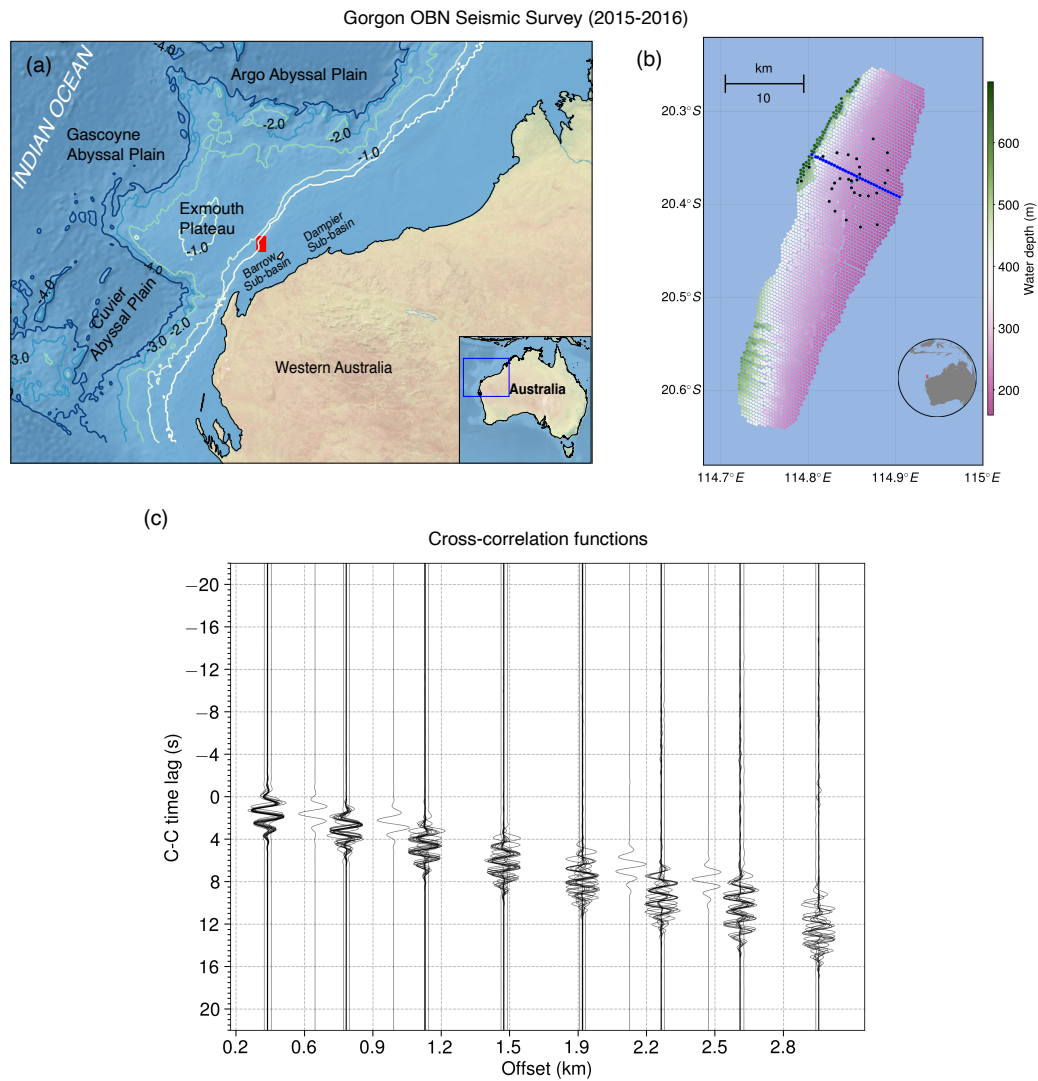


**Figure 1.** Map of the ocean bottom seismic survey in Western Australia and cross-correlation (CC) functions from ambient noise interferometry. (a) Ocean Bottom Node (OBN) seismic survey in the Gorgon gas field offshore Western Australia by Chevron Australia and its partners. (b) Zoom-in of the red rectangle in (a). Each dot refers to an OBN with the color suggesting water depth. The line of node with the blue color indicates Line 3924 used in the study. The OBNs on the three spiral arms in the black color are used for beamforming analysis of mapping ambient noise sources. (c) CC functions for Line 3924 sorted by offsets (the distance between a station pair) from Hour 15 of Julian Day 1, 2016. We limit the CC functions to 3 km offset.

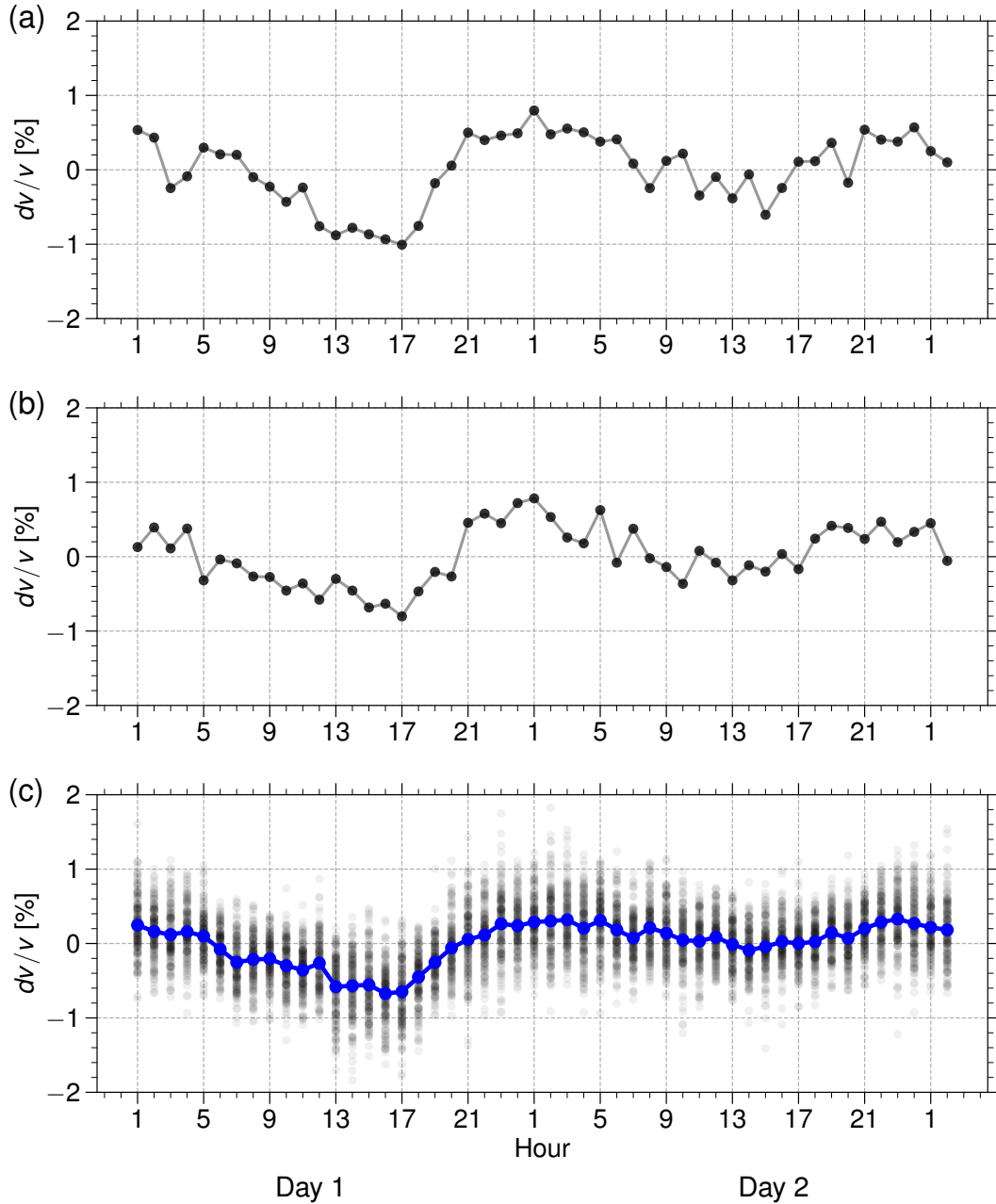


**Figure 2.** The relative seismic velocity changes ( $dv/v$ ) in time during the passive monitoring period of Julian Day 1 and 2, 2016. The velocity changes are estimated from the direct arrivals of Scholte waves in the CC functions of station pairs in Line 3924 (Figure 1). (a) and (b) depict the  $dv/v$  from two station pairs, with station distances of 1.2 km and 2.4 km. (c) shows the velocity changes from all the station pairs (with a maximum offset 3.2 km) in Line 3924. Each black dot is the  $dv/v$  from a station pair measurement. The blue curve in (c) is the average  $dv/v$ .

195 We sort the CC functions of all the station pairs into common-station gathers. Each  
 196 common-station gather can be considered as a seismic common-source gather so that the  
 197 shared common station is the virtual source for generating seismic waves, and the rest  
 198 of the stations from the selected survey line are the receivers. Figure 3 contains common-  
 199 station gathers of the reference data and the monitoring data from Hour 15 of Day 1 (Fig-

200 ure 3a) and Hour 1 of Day 2 (Figure 3b). We observe that the main difference between  
 201 the reference and monitoring data of different hours is in the arrival times of the Scholte  
 202 waves. Scholte waves from Hour 15 of Day 1 arrive later than the reference data (Fig-  
 203 ures 3a and 3c), indicating a velocity decrease than the reference model, while those from  
 204 Hour 1 of Day 2 arrive at an earlier time than the reference data (Figures 3b and 3d),  
 205 suggesting a velocity increase. The observations from the common-station gathers are  
 206 consistent with the velocity changes in Figure 2.

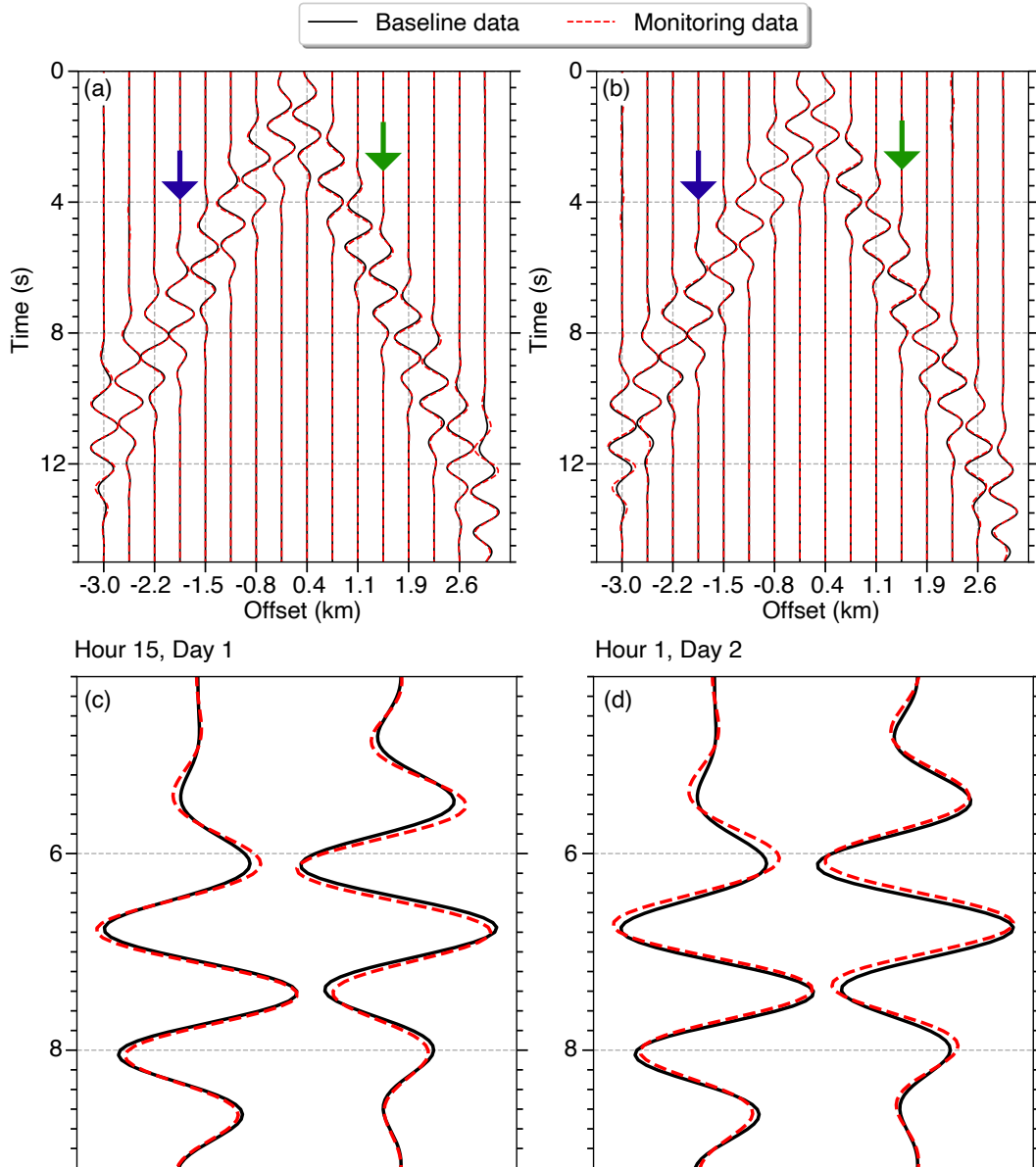


**Figure 3.** Common-station gathers sorted from CC functions of station pairs of Line 3924. (a) is the comparison of the reference data (solid black curve) and the monitoring data (dashed red curve) of Hour 15 Day 1. (b) is the comparison of the reference data (solid black curve) and the monitoring data (dashed red curve) of Hour 1 Day 2. (c) and (d) are closeups of the seismic traces at -1.9 km and 1.5 km offsets (from left to right, indicated by the blue and green arrows, respectively) from (a) and (b).

207 Previous studies have extensively utilized coda waves from ambient noise interfer-  
208 ometry to monitor  $dv/v$  (e.g. Sens-Schönfelder & Wegler, 2006; Brenguier et al., 2008;  
209 Obermann, Schimmel, et al., 2013; Richter et al., 2014; Clements & Denolle, 2018; Takano  
210 et al., 2019). Multiply scattered wave propagation results in a more diffused noise wave-  
211 field than direct arrivals, making it less sensitive to the ambient noise source variations  
212 in time (Colombi et al., 2014; Mao et al., 2019). In contrast, the direct Scholte waves  
213 can exhibit greater sensitivity to the ambient noise source distribution and azimuthal  
214 variation over time (Weaver et al., 2009; Colombi et al., 2014; Takano et al., 2020). There-  
215 fore, it is crucial to verify that the observed waveform changes are from subsurface phys-  
216 ical property changes, rather than being linked to variations in the ambient noise sources.  
217 We employ the beamforming method (Bucker, 1976; Bowden et al., 2021; Igel et al., 2023)  
218 to map the seafloor ambient noise source on an hourly basis. In order to maximize the  
219 potential resolution of the imaged source distribution of the incoming noise wavefield,  
220 we select the OBNs with a spiral-arm geometrical configuration (Figure 1c) (Kennett et  
221 al., 2015). Figure 4 displays the seafloor ambient noise sources during selected hours of  
222 Day 1, 2016. Throughout the monitoring periods, we observe consistent and stable amb-  
223 ient noise sources, with most of the energy concentrated in the south-east direction, par-  
224 allel to the chosen line direction for cross correlation. The distribution of ambient noise  
225 source is consistent with the asymmetry in the cross-correlation functions (Figure 2). The  
226 mapped seafloor noise source has an apparent slowness of about 5 s/km (velocity of 0.2  
227 km/s). Figure 5 shows the dominant azimuths of the incoming noise field during the two-  
228 day monitoring periods, calculated using the slowness vectors at the center-of-mass of  
229 the beamforming results, with a maximum perturbation of  $\pm 1^\circ$  around an azimuth of  
230  $123^\circ$  (from the north direction). Hence, we suggest that the seafloor ambient noise source  
231 during the entire monitoring period is stable. The observed time-lapse seismic velocity  
232 changes, derived from the extracted repetitive Scholte waves from seafloor ambient noise,  
233 are associated with time-lapse changes in the shear-wave velocity of the seafloor.



234

### 3.2 High-resolution reference model estimation: full waveform inversion

235

236

237

238

The dense array of OBNs provides the opportunity for computing time-lapse quantitative images of seafloor velocity changes, i.e., localizing the temporal velocity changes in the subsurface in 2-D along node lines, from the continuous recordings of ambient noise using high-resolution waveform inversion technique.

239

240

241

242

243

244

245

246

247

248

249

250

251

252

253

A reference velocity model is necessary for estimating and comparing time-lapse subsurface models. We use the full waveform inversion (FWI) (Tarantola, 1984; Shipp & Singh, 2002; Guo et al., 2022) technique to estimate a high-resolution reference model using the extracted Scholte waves. In the numerical implementation, a gradient-based linearized inversion approach is used to update the velocity model iteratively with the aim of minimizing the misfit between synthetic and observed data, with the gradients of the data misfit to model parameters efficiently calculated by the adjoint-state method from the cross-correlation of the source and adjoint wavefields (Tarantola, 1984; Tromp et al., 2005; Fichtner et al., 2006). The source and adjoint wavefields can be obtained by source-wavelet generated forward wave propagation and adjoint-source generated backward wave propagation (Shipp & Singh, 2002). We use time-domain staggered-grid finite-difference with fourth-order spatial and second-order temporal accuracy to solve the elastic-wave equation in stress and particle-velocity formulation (Virieux, 1986). The grid spacing for the finite-difference was 25 m. A Gaussian smoothing operator with 200 m horizontal and 50 m vertical lengths was applied to the gradient for regularization.

254

255

256

257

We use the reference data in the form of common-station gathers (e.g., Figure 3) as the observed data for the reference FWI. Considering that the phase information in the virtual Scholte waves of the CC functions is more reliable than the amplitude, we employ a trace-normalized FWI method (Shen, 2010), with the misfit function  $J$ :

$$J = \sum_{i=1}^{N_s} \sum_{j=1}^{N_r} \left\| \frac{\mathbf{s}_{i,j}}{\|\mathbf{s}_{i,j}\|} - \frac{\mathbf{d}_{i,j}}{\|\mathbf{d}_{i,j}\|} \right\|^2, \quad (1)$$

258

259

260

where  $\mathbf{s}_{i,j}$  and  $\mathbf{d}_{i,j}$  are seismic traces (1-D time-series vectors) from the synthetic and field data respectively,  $\| \cdot \|$  is the L-2 norm,  $i$  and  $j$  are the indexes for the sources and receivers,  $N_s$  and  $N_r$  are the number of sources and receivers.

261

The associated adjoint source that is used for adjoint wavefield propagation is

$$J = \left( \frac{\delta \mathbf{d}_{i,j}}{\|\mathbf{s}_{i,j}\|} \right) - \left( \frac{\delta \mathbf{d}_{i,j}^T \cdot \mathbf{d}_{i,j}}{\|\mathbf{s}_{i,j}\|^2} \frac{\mathbf{s}_{i,j}}{\|\mathbf{s}_{i,j}\|} \right), \quad (2)$$

262

where  $\delta \mathbf{d}_{i,j} = \mathbf{s}_{i,j} - \mathbf{d}_{i,j}$  and  $T$  is the transpose operator.

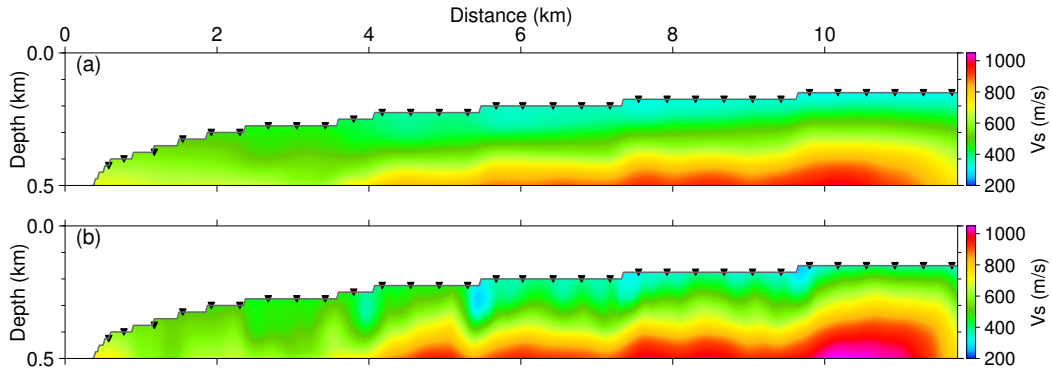


**Figure 6.** Shear-wave velocity models of the shallow seafloor. (a) Velocity model estimated from wave-equation dispersion inversion (Chen & Saygin, 2022); (b) velocity model estimated from the trace-normalized FWI method, using (a) as the starting model. The black triangles in (a) indicate the OBNs, with a spacing of  $\sim 300$  m.

263 Figure 6a shows the shear-velocity model from the wave-equation dispersion inver-  
 264 sion, which uses the adjoint-state method for fitting the surface wave disper-  
 265 sion spectra (Li et al., 2017; Chen & Saygin, 2022). With the model in Figure 6a as the starting  
 266 model, Figure 6b shows the velocity model obtained from the reference inversion using  
 267 trace-normalized FWI after 50 iterations. The data misfit has been reduced significantly  
 268 after FWI (Figure S4). The synthetic data after the FWI show a much better match (Fig-  
 269 ure S5) to the reference Scholte wave arrivals than those from the original tomographic  
 270 model (Figure 6a). The velocity model in Figure 6b is used as the reference model for  
 271 computing time-lapse seafloor models in the next section.

### 272 **3.3 Localizing time-lapse velocity changes: wave-equation double-difference** 273 **inversion**

274 The most straightforward approach for extending seismic inversion to time-lapse  
 275 monitoring entails conducting separate inversions for the reference and monitoring data.  
 276 However, seismic inversion is usually a highly nonlinear problem, especially in the con-  
 277 text of FWI (Tarantola, 1984; Shipp & Singh, 2002; Guo et al., 2021). The convergence  
 278 level of seismic inversion of individual data can be different, as a result the model dif-  
 279 ference introduced by different local minima in successive inversions may generate mis-  
 280 leading time-lapse subsurface models (Yang et al., 2016). In contrast, double-difference  
 281 waveform inversion (DD-WI) (Denli & Huang, 2009; Zheng et al., 2011) directly inverts  
 282 for the difference between reference and monitoring waveform data. This approach has  
 283 been demonstrated for enhancing the reliability of time-lapse subsurface velocity mod-  
 284 els, with case studies utilizing body waves from controlled active seismic sources for imag-  
 285 ing velocities changes (Yang et al., 2016; Zhou & Lumley, 2021).

286 Analysis of the ambient noise sources throughout the monitoring period indicates  
 287 that the observed time-lapse changes stem from alterations in subsurface properties rather  
 288 than temporal variations in the ambient noise source. The time-lapse difference of the  
 289 extracted Scholte waves mainly manifests in variations of travel times (Figure 3). This  
 290 observation implies that an objective function for the seismic time-lapse inversion prob-  
 291 lem using arrival time differences (shifts) between the monitoring and reference data may  
 292 be more suitable for quantifying the time-lapse velocity models than including the com-  
 293 plete waveform details in the inversion. Elastic wave equation based double-difference  
 294 inversion (EW-DD) using travel time differences as an objective function has been pro-

295 posed before, but in the context of seismic adjoint tomography for estimating seismic wave  
 296 velocity structures, where the differential measurements are constructed between receivers  
 297 (Yuan et al., 2016). We introduce this approach for time-lapse inversion based on elas-  
 298 tic wave equation, where the differential measurements are constructed between refer-  
 299 ence and monitoring data.

300 Here, we propose the EW-DD method using travel time differences of the direct  
 301 Scholte waves to obtain time-lapse velocity models using the extracted Scholte waves from  
 302 ambient noise. The misfit function is defined as

$$J = \sum_{i=1}^{Ns} \sum_{j=1}^{Nr} \|\Delta t_{i,j}^d - \Delta t_{i,j}^s\|^2, \quad (3)$$

303 where  $\Delta t_{(i,j)}^d$  is the travel time difference between the monitoring and the refer-  
 304 ence observed data, and  $\Delta t_{(i,j)}^s$  is the travel time difference between the synthetic data  
 305 from the monitoring model and the reference FWI model.  $i$  and  $j$  are the indexes for the  
 306 sources and receivers,  $Ns$  and  $Nr$  are the number of sources and receivers. The time dif-  
 307 ference (shift) can be estimated by comparing waveform data using cross correlation. The  
 308 term ‘double-difference’ comes from the two-level differences in equation 3: (1) the dif-  
 309 ference between reference and monitoring data, either synthetic or observed, and (2) the  
 310 difference between the synthetic and observed measurements from (1).

311 The adjoint source for the EW-DD of travel time differences (Yuan et al., 2016),  
 312 which is used for elastic wave propagation in backward time steps for computing the ad-  
 313 joint wavefields, can be derived as

$$\chi_{i,j} = (\Delta t_{i,j}^d - \Delta t_{i,j}^s) \partial_t s_{i,j}(t - \Delta t_{i,j}^s), \quad (4)$$

314 where  $s_{i,j}$  is a seismic waveform trace (1-D time-series vector) from the synthetic  
 315 data. The only difference with the DD-WI is the adjoint source. Both the reference and  
 316 time-lapse inversion methods honor the seafloor bathymetry which is implicitly included  
 317 when solving the elastic-wave equation.

318 We apply the EW-DD method to differential measurements of monitoring and refer-  
 319 ence data to localize the shear-wave velocity changes in the seafloor on an hourly ba-  
 320 sis. We use the same inversion parameters, as described in the previous section for refer-  
 321 ence waveform inversion, in the time-lapse inversion. The misfit has been significantly  
 322 reduced after the inversion (Figure S6). Figure 7 shows the time-lapse velocity differ-  
 323 ence between the reference model and the velocity models of selected hours at Day 1 and  
 324 2, in the horizontal and depth domain. The changes in Figure 7b and 7c are overall neg-  
 325 ative suggesting a slower velocity than the reference model, while the velocity changes  
 326 in the remaining panels of Figure 7 are mainly positive indicating a faster velocity than  
 327 the reference. The inferred negative/positive patterns in space are in agreement with Fig-  
 328 ures 2 and 3. The changes are more noticeable in Figure 7c than those in Figure 7b, con-  
 329 sistent with Figure 2 (also Figure S7). We also apply the inversion method to the mon-  
 330 itoring data from further survey lines (Figures S9, S10); the localized time-lapse veloc-  
 331 ity changes of the seafloor show consistent increasing/decreasing patterns with Figure  
 332 S2.

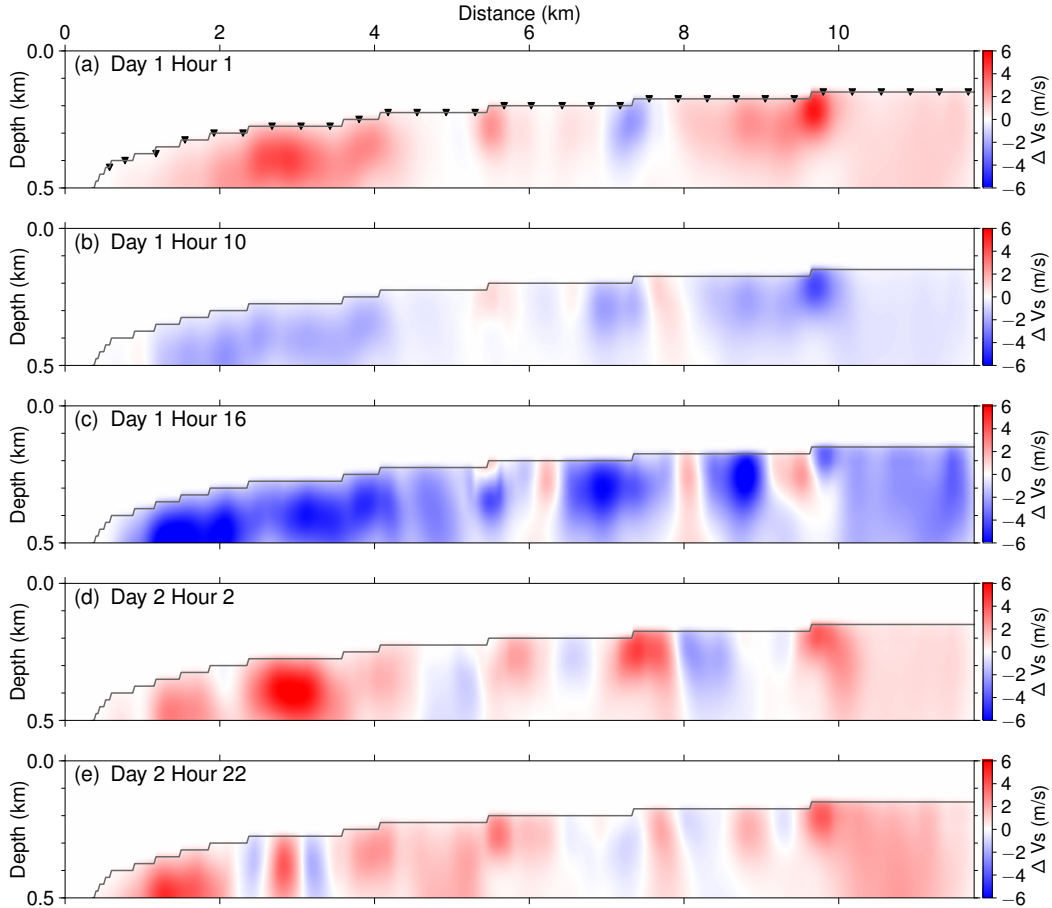


**Figure 7.** Time-lapse subsurface models of velocity changes compared with the reference model (Figure 6b), from selected hours during the two-day monitoring period. The black triangles in (a) indicate the locations of OBNs.

333

### 3.4 Resolution analysis of double-difference inversion using Scholte waves

334

335

336

337

338

339

340

341

342

343

344

345

346

347

348

349

350

351

The observed temporal velocity changes are subtle, especially when compared with the likely difference between the reference model from FWI and the ground truth of the seafloor. It is important to verify if these velocity changes are real, not artifacts coming from unfitted data in the reference inversion. Therefore we perform a series of synthetic tests, including errors in the reference model and noise in the reference and time-lapse data. We use the same frequency range, recording geometry and inversion parameters of the field data for these tests. The model in Figure 6b is used as the ‘true’ reference model for generating the ‘observed’ reference data. We then add 1% positive and negative Gaussian-shaped velocity anomalies (‘time-lapse velocity changes’, with 1 km horizontal extent and 0.2 km thickness, Figure 8a) to the reference model (Figure 6b) to generate the ‘observed’ monitoring data. We then add noise to the reference and monitoring data, respectively, so that the signal to noise ratio (S/N) is  $\sim 8$ , lower than that of the extracted hourly CC functions (Figure 1c). The tomographic velocity model in Figure 6a, which contains much larger difference with the ‘true’ reference model than the added velocity anomalies, is then used as the starting model for the DD inversion. The recovered velocity changes are shown in Figure 8e. We also apply the same inversion workflow to velocity anomalies with a lower magnitude (0.5%, Figures 8b) and anomalies of different sizes (Figures 8c and 8d), with the inversion results shown in Figures 8f-

352 8h, respectively. In Figures 8c and 8d where the anomalies are smaller, the estimated  
 353 anomalies (Figures 8g and 8h) from the DD inversion still provide a favorable match to  
 354 the true model, although their features are relatively less well constrained. The data also  
 355 has less resolution for the anomalies in the deeper part of the model (Figure 8g). The  
 356 anomalies are better constrained in the horizontal direction than in the vertical direc-  
 357 tions, because the Scholte waves dominantly propagate along the seabed interface. The  
 358 inversion results suggest that the proposed method is robust to errors in the reference  
 359 model and data noise. The data can resolve subtle velocity changes on the scale of 0.5-  
 360 1 km laterally, and  $\sim 200$  m vertically.

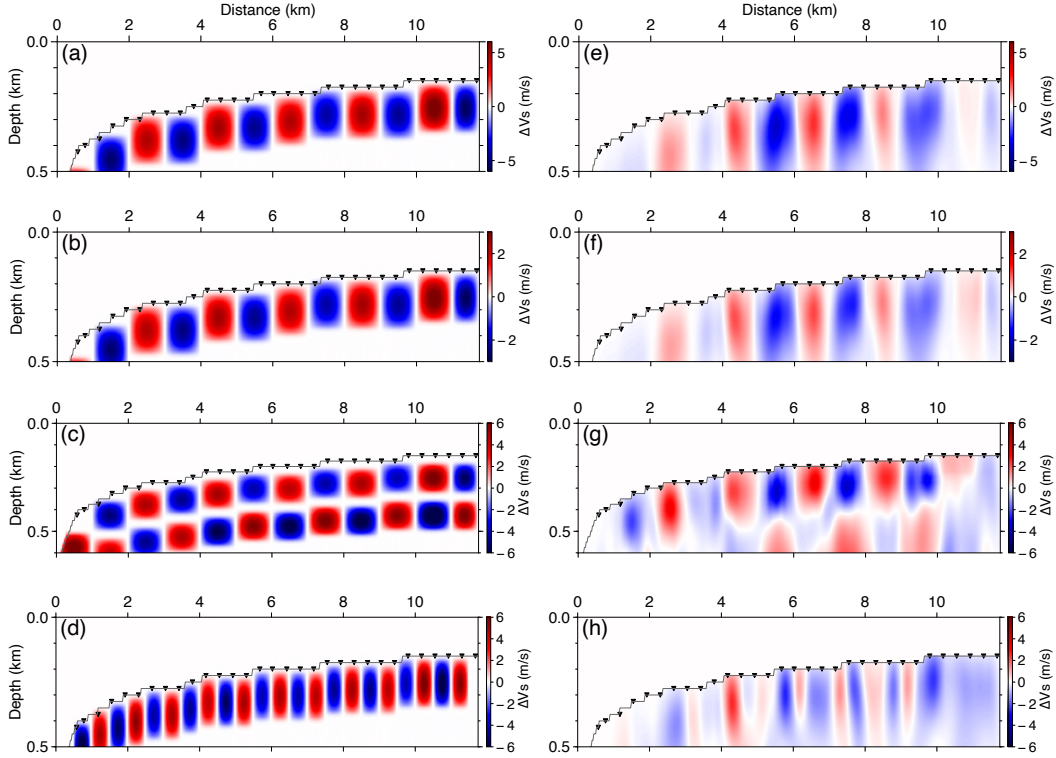


**Figure 8.** Checkerboard test for time-lapse wave-equation double-difference inversion. The velocity anomalies (time-lapse velocity changes) in (a) have a size of 1 km and 0.2 km horizontally and vertically, respectively, with magnitude of 1%, (b) have the same size but magnitude of 0.5%, (c) have a size of 1 km and 0.1 km horizontally and vertically, and (d) have a size of 0.5 km and 0.2 km horizontally and vertically. (e)-(h) show the recovered velocity anomalies from time-lapse inversion using Scholte waves. The black triangles at the seafloor indicate the locations of OBSs.

#### 361 4 Discussion

362 The phenomenon of temporal variation in seismic velocity is ubiquitous and has  
 363 been associated with different physical mechanisms. For example, both velocity increase  
 364 (Wegler et al., 2006; Yates et al., 2019) and decrease (Brenguier et al., 2008; Obermann,  
 365 Schimmel, et al., 2013) have been observed before the eruption of volcanos, indicating  
 366 distinct deformational styles depending on the position of the pressure source (Yates et  
 367 al., 2019). On the other hand, velocity changes with a periodic pattern tend to be re-

lated to environmental factors, such as climatic perturbations including temperature (Richter et al., 2014; Sens-Schönfelder & Eulendorf, 2019) and precipitation (Sens-Schönfelder & Wegler, 2006; Oakley et al., 2021; Mao et al., 2022), and the gravitational field of the Sun and Moon resulting in tidal deformation, comprising of solid earth tide and ocean tide loading (De Fazio et al., 1973; Yamamura et al., 2003; Hillers et al., 2015; Takano & Nishida, 2023). Such perturbations cause strain changes in the subsurface rock, leading to the changes in the velocity of the seismic waves. In recent years, emerging monitoring techniques using seismic ambient noise allow continuous and real-time monitoring of seismic velocity variations in a cost-effective and eco-friendly way (Sens-Schönfelder & Wegler, 2006; Donaldson et al., 2017). Takano et al. (2014) revealed onshore seismic shear-wave velocity decrease of 0.1-0.3% caused by solid earth tide during crustal dilatation compared with that from the contraction episodes. The opening and closure of cracks or pores in rocks induced by strain changes lead to velocity decrease and increase, respectively (Yamamura et al., 2003; Takano et al., 2014). Mao et al. (2019) presented seismic velocity monitoring with hourly temporal resolution using a dense array of seismometers and suggest that the diurnal  $dv/v$  changes are likely induced by a superposition of tidal and thermal effects. The tidal-induced velocity changes are usually constrained to the shallow crust (Hillers et al., 2015). Moreover, large temporal velocity changes up to 1% (Takano & Nishida, 2023) have been observed in the low shear-wave velocity region of the shallow crust using hourly stacked ambient noise auto-correlations, which have been associated with the solid earth tide. Notably, this study suggests that the response of seismic velocity to strain changes becomes more sensitive when the shear-wave velocity is low (Takano & Nishida, 2023), resulting in increasing relative velocity changes with decreasing shear-wave velocity. The strain-velocity sensitivity varies from approximately  $10^3$  to  $10^5$  in Takano and Nishida (2023). This could explain the observed much smaller velocity changes induced by tidal deformation from previous studies, for example, the magnitude of  $dv/v$  is about 0.08% at the Piton de la Fournaise volcano, where the subsurface velocity is higher than that of the sedimentary layers (Mordret et al., 2015). In addition, recent studies also revealed periodic seismic velocity variations at the order of 0.01% associated with atmospheric pressure changes (Gradon et al., 2021; Kramer et al., 2023).

Studies for time-lapse seafloor seismic velocity are relatively rare compared with those of the continental (onshore) crust. We observe up to 0.8% shear-wave velocity change in the seafloor, which contains thick sediments with low shear-wave velocities (Figure 6) and as a result high strain-velocity sensitivity (Takano & Nishida, 2023). Figure 9 shows the comparison of the time-lapse velocity changes with the variations of the sea level height measured on a pressure inverted echo sounder about 8 km away. The velocity exhibits an inversely correlation with the sea level height, i.e., the velocity decreases with increasing sea level. This observation contradicts the expectation that increasing confining stress (e.g. higher sea level) results in the closing of cracks or pores in the subsurface, which leads to an increase in seismic velocity (Takano et al., 2014). Hillers et al. (2015) observed similar phenomenon from onshore vertical component coda waves, that the velocity of seismic waves reduces during periods of volumetric compression induced by solid earth tide loading. This seemingly surprising decrease in velocity with increasing confining stress is indeed compatible with previous resonant bar experiments using relatively porous, compliant rock samples characterized by very low seismic velocities (Zinszner et al., 1997; Pasqualini et al., 2007). The porous seafloor with low seismic velocities here could be comparable to the onshore shallow crust with weathered, almost totally decomposed granodiorite which grades into grus and corestones near the San Jacinto Fault in Hillers et al. (2015). The porous, low velocity material can experience dilatancy from inelastic damage under compression, resulting in decreasing seismic velocities, which implies a different response to cyclic deformation compared to more compact, solidified rocks (Zinszner et al., 1997; Pasqualini et al., 2007). Moreover, using active-source seismic experiments with piezoelectric transducer as the source, Yamamura et al. (2003) found diurnal variations in the inland seismic velocity with an amplitude of 0.3% about 20 m from the coast,

423 which also anti-correlates in pattern and phase with the in-situ areal strain and sea level  
 424 heights, while the role of the solid earth tide is negligible. Other recent studies show re-  
 425 duced seismic velocity in a sea levee (Planès et al., 2017) and a sea dike (Joubert et al.,  
 426 2018) when the sea level is high. The underlying mechanism involves infiltrated water  
 427 at high sea levels raising in-situ pore-water pressure, which subsequently reduces effec-  
 428 tive stress and shear-wave velocity (Planès et al., 2017; Joubert et al., 2018). Kramer  
 429 et al. (2023) suggest that in saturated conditions (e.g. at the seafloor), when cracks close  
 430 from increasing stress, the fluid within is pushed to the pores, which leads to an over-  
 431 all increase of the pore pressure and a decrease of seismic velocity. Furthermore, Andajani  
 432 et al. (2022) found that the correlation between sea level height and nearby inland seis-  
 433 mic velocity changes can be negative or positive, depending on the in-situ local stress,  
 434 orientation of dominant crack, and hydraulic conductivity. The local heterogeneities (Andajani  
 435 et al., 2022) in the seafloor could also be the reason for the observed negative anom-  
 436 alies in the time-lapse seafloor images (Figure 7) associated with positive velocity changes  
 437 and the positive anomalies in the images corresponding to negative velocity changes, al-  
 438 though we acknowledge that some of the anomalies could also be beyond the resolution of  
 439 seismic inversion. Taken together, the time-lapse velocity variations in the seafloor could  
 440 be related to dilatant effects for porous, low velocity shallow seafloor and the pore pres-  
 441 sure changes associated with sea level. We also acknowledge that the short passive moni-  
 442 toring period of two days, limited by the data acquisition in this study, hinder a com-  
 443 plete and comprehensive study of the seafloor property time-lapse changes with environ-  
 444 mental factors such as sea level heights. Future studies should use at least a few months  
 445 of data (Yamamura et al., 2003).

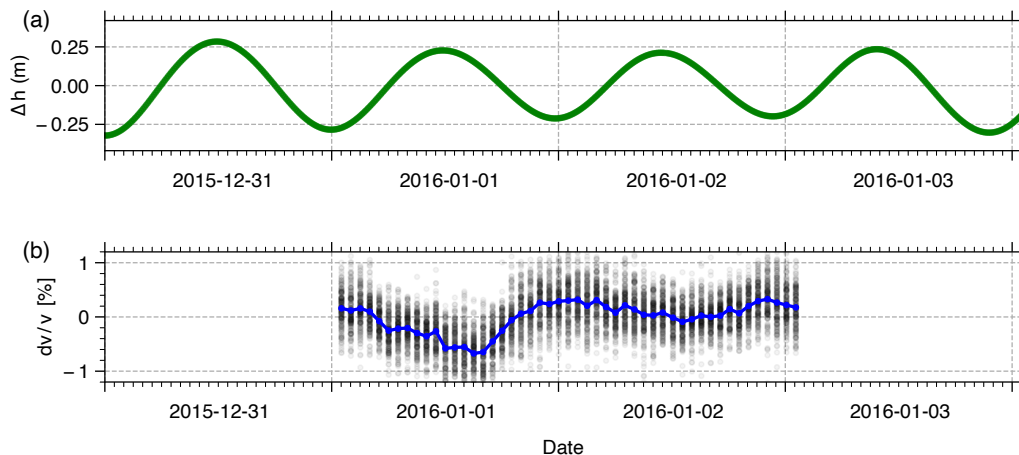


**Figure 9.** A comparison of (a) the sea level heights and (b) the time-lapse relative seismic velocity changes ( $dv/v$ ). (a) was measured using a pressure inverted echo sounder about 8 km away from the survey line 3924, then zero-phase bandpass filtered around 1 cycle per day. (b) is the same with Figure 2c.

## 446 5 Conclusion

447 In this study, we propose a passive space-time monitoring technique for real-time  
 448 tracking of subsurface property changes with high temporal (hourly) and spatial (hun-  
 449 dreds of meters) resolution. Using seismic ambient noise data recorded by a dense ar-  
 450 ray of ocean bottom nodes offshore Western Australia, we detect temporal variations of  
 451 shear-wave velocity of up to 0.8% in the seafloor, with a likely 24-hour cycling pattern.

452 The velocity seems inversely correlated with sea level height, decreasing with increas-  
 453 ing sea level, possibly associated with dilatant effects for porous, low-velocity shallow seafloor  
 454 and rising pore pressure with high sea level. To localize the velocity changes in the sub-  
 455 surface, we first build a high-resolution reference seafloor model from FWI of Scholte waves.  
 456 Then using the double difference of arrival time differences between reference and mon-  
 457 itoring data, we obtain quantitative time-lapse seafloor images in the horizontal and depth  
 458 domain containing the heterogeneous relative velocity variations. The elastic-wave equa-  
 459 tion based workflow from building a high-resolution reference model to time-lapse inver-  
 460 sion using Scholte wave measurements honors the full wave physics, is robust to data noise  
 461 and errors from the reference model, and is sensitive to subtle velocity changes. A com-  
 462 parable approach can be applied to passive seismic data from dense seismic arrays and  
 463 Distributed Acoustic Sensing (DAS) for real-time monitoring of groundwater level, vol-  
 464 cano, subduction zone and CO<sub>2</sub> capture storage, in the aim for an in-depth understand-  
 465 ing of the evolving 4-D Earth.

## 466 Open Research Section

467 The data used for reproducing the figures, including the hourly CC functions,  $dv/v$   
 468 measurements and seismic velocity models, are publicly available at <https://doi.org/10.5281/zenodo.6804990>.

## 469 Acknowledgments

470 This research was funded by the Deep Earth Imaging Future Science Platform, CSIRO.  
 471 This work was supported by resources provided by the Pawsey Supercomputing Centre  
 472 with funding from the Australian Government and the Government of Western Australia.  
 473 The raw seismic data of the Gorgon Ocean Bottom Node Seismic Survey (ID: ENO0603054)  
 474 can be requested from the National Offshore Petroleum Information Management Sys-  
 475 tem (NOPIMS) via contacting [AusGeoData@ga.gov.au](mailto:AusGeoData@ga.gov.au). We thank Chevron Australia  
 476 for their assistance with the data.

## 477 References

- 478 Andajani, R. D., Tsuji, T., Snieder, R., & Ikeda, T. (2022). Spatial and temporal  
 479 influence of sea level on inland stress based on seismic velocity monitoring.  
 480 *Earth, Planets and Space*, *74*(1), 97.
- 481 Ardhuin, F., Gualtieri, L., & Stutzmann, E. (2015). How ocean waves rock the  
 482 Earth: Two mechanisms explain microseisms with periods 3 to 300 s. *Geophys-  
 483 ical Research Letters*, *42*(3), 765–772.
- 484 Arts, R., Eiken, O., Chadwick, A., Zweigel, P., Van Der Meer, B., & Kirby, G.  
 485 (2004). Seismic monitoring at the Sleipner underground CO<sub>2</sub> storage site  
 486 (North Sea). *Geological Society, London, Special Publications*, *233*(1), 181–  
 487 191.
- 488 Barreyre, T., Parnell-Turner, R., Wu, J.-N., & Fornari, D. (2022). Tracking crustal  
 489 permeability and hydrothermal response during seafloor eruptions at the East  
 490 Pacific Rise, 9 50'N. *Geophysical Research Letters*, *49*(3), e2021GL095459.
- 491 Batzle, M., & Wang, Z. (1992). Seismic properties of pore fluids. *Geophysics*,  
 492 *57*(11), 1396–1408.
- 493 Bensen, G., Ritzwoller, M., Barmin, M., Levshin, A. L., Lin, F., Moschetti, M.,  
 494 ... Yang, Y. (2007). Processing seismic ambient noise data to obtain reli-  
 495 able broad-band surface wave dispersion measurements. *Geophysical journal  
 496 international*, *169*(3), 1239–1260.
- 497 Bowden, D. C., Sager, K., Fichtner, A., & Chmiel, M. (2021). Connecting beam-  
 498 forming and kernel-based noise source inversion. *Geophysical Journal Interna-  
 499 tional*, *224*(3), 1607–1620.
- 500 Brenguier, F., Campillo, M., Takeda, T., Aoki, Y., Shapiro, N., Briand, X., ...

- 501 Miyake, H. (2014). Mapping pressurized volcanic fluids from induced crustal  
502 seismic velocity drops. *Science*, *345*(6192), 80–82.
- 503 Brenguier, F., Courbis, R., Mordret, A., Campman, X., Boué, P., Chmiel, M., ...  
504 others (2020). Noise-based ballistic wave passive seismic monitoring. part 1:  
505 body waves. *Geophysical Journal International*, *221*(1), 683–691.
- 506 Brenguier, F., Rivet, D., Obermann, A., Nakata, N., Boué, P., Lecocq, T., ...  
507 Shapiro, N. (2016). 4-D noise-based seismology at volcanoes: Ongoing ef-  
508 forts and perspectives. *Journal of Volcanology and Geothermal Research*, *321*,  
509 182–195.
- 510 Brenguier, F., Shapiro, N. M., Campillo, M., Ferrazzini, V., Duputel, Z., Coutant,  
511 O., & Nercessian, A. (2008). Towards forecasting volcanic eruptions using  
512 seismic noise. *Nature Geoscience*, *1*(2), 126–130.
- 513 Bucker, H. P. (1976). Use of calculated sound fields and matched-field detection to  
514 locate sound sources in shallow water. *The Journal of the Acoustical Society of*  
515 *America*, *59*(2), 368–373.
- 516 Campillo, M., & Paul, A. (2003). Long-range correlations in the diffuse seismic coda.  
517 *Science*, *299*(5606), 547–549.
- 518 Castellanos, J. C., Clayton, R. W., & Juarez, A. (2020). Using a time-based  
519 subarray method to extract and invert noise-derived body waves at Long  
520 Beach, California. *Journal of Geophysical Research: Solid Earth*, *125*(5),  
521 e2019JB018855.
- 522 Chen, Y., & Saygin, E. (2022). 3D S wave imaging via robust neural network in-  
523 terpolation of 2D profiles from wave equation dispersion inversion of seismic  
524 ambient noise. *Journal of Geophysical Research: Solid Earth*, e2022JB024663.
- 525 Clarke, D., Zaccarelli, L., Shapiro, N., & Brenguier, F. (2011). Assessment of reso-  
526 lution and accuracy of the Moving Window Cross Spectral technique for mon-  
527 itoring crustal temporal variations using ambient seismic noise. *Geophysical*  
528 *Journal International*, *186*(2), 867–882.
- 529 Clements, T., & Denolle, M. A. (2018). Tracking groundwater levels using the ambi-  
530 ent seismic field. *Geophysical Research Letters*, *45*(13), 6459–6465.
- 531 Colombi, A., Chaput, J., Brenguier, F., Hillers, G., Roux, P., & Campillo, M.  
532 (2014). On the temporal stability of the coda of ambient noise correlations.  
533 *Comptes Rendus Geoscience*, *346*(11-12), 307–316.
- 534 De Fazio, T. L., Aki, K., & Alba, J. (1973). Solid earth tide and observed change  
535 in the in situ seismic velocity. *Journal of Geophysical Research*, *78*(8), 1319–  
536 1322.
- 537 Denli, H., & Huang, L. (2009). Double-difference elastic waveform tomography in  
538 the time domain. In *2009 seg annual meeting*.
- 539 de Ridder, S., & Biondi, B. (2013). Daily reservoir-scale subsurface monitoring using  
540 ambient seismic noise. *Geophysical Research Letters*, *40*(12), 2969–2974.
- 541 de Ridder, S., Biondi, B., & Clapp, R. (2014). Time-lapse seismic noise correlation  
542 tomography at Valhall. *Geophysical Research Letters*, *41*(17), 6116–6122.
- 543 Donaldson, C., Caudron, C., Green, R. G., Thelen, W. A., & White, R. S. (2017).  
544 Relative seismic velocity variations correlate with deformation at Kīlauea  
545 volcano. *Science advances*, *3*(6), e1700219.
- 546 Fichtner, A., Bunge, H.-P., & Igel, H. (2006). The adjoint method in seismology: I.  
547 theory. *Physics of the Earth and Planetary Interiors*, *157*(1-2), 86–104.
- 548 Fokker, E., Ruigrok, E., Hawkins, R., & Trampert, J. (2023). 4D physics-based pore  
549 pressure monitoring using passive image interferometry. *Geophysical Research*  
550 *Letters*, *50*(5), e2022GL101254.
- 551 Gradon, C., Brenguier, F., Stammeijer, J., Mordret, A., Hindriks, K., Campman, X.,  
552 ... Chmiel, M. (2021). Seismic velocity response to atmospheric pressure using  
553 time-lapse passive seismic interferometry. *Bulletin of the Seismological Society*  
554 *of America*, *111*(6), 3451–3458.
- 555 Gualtieri, L., Bachmann, E., Simons, F. J., & Tromp, J. (2020). The origin of sec-

- 556           ondary microseism Love waves. *Proceedings of the National Academy of Sci-*  
557           *ences*, 117(47), 29504–29511.
- 558 Guo, P., Singh, S., Vaddineni, V., Grevemeyer, I., & Saygin, E. (2022). Lower  
559           oceanic crust formed by in situ melt crystallization revealed by seismic layer-  
560           ing. *Nature Geoscience*, 15, 591–596.
- 561 Guo, P., Singh, S. C., Vaddineni, V. A., Visser, G., Grevemeyer, I., & Saygin, E.  
562           (2021). Nonlinear full waveform inversion of wide-aperture OBS data for Moho  
563           structure using a trans-dimensional bayesian method. *Geophysical Journal*  
564           *International*, 224(2), 1056–1078.
- 565 Hadziioannou, C., Larose, E., Baig, A., Roux, P., & Campillo, M. (2011). Improving  
566           temporal resolution in ambient noise monitoring of seismic wave speed. *Jour-*  
567           *nal of Geophysical Research: Solid Earth*, 116(B7).
- 568 Hasselmann, K. (1963). A statistical analysis of the generation of microseisms. *Re-*  
569           *views of Geophysics*, 1(2), 177–210.
- 570 Hicks, E., Hoerber, H., Houbiers, M., Lescoffit, S. P., Ratcliffe, A., & Vinje, V.  
571           (2016). Time-lapse full-waveform inversion as a reservoir-monitoring tool—a  
572           North Sea case study. *The Leading Edge*, 35(10), 850–858.
- 573 Hillers, G., Retailleau, L., Campillo, M., Inbal, A., Ampuero, J.-P., & Nishimura,  
574           T. (2015). In situ observations of velocity changes in response to tidal de-  
575           formation from analysis of the high-frequency ambient wavefield. *Journal of*  
576           *Geophysical Research: Solid Earth*, 120(1), 210–225.
- 577 Igel, J. K., Bowden, D. C., & Fichtner, A. (2023). SANS: Publicly available daily  
578           multi-scale seismic ambient noise source maps. *Journal of Geophysical Re-*  
579           *search: Solid Earth*, 128(1), e2022JB025114.
- 580 Joubert, A., Le Feuvre, M., & Côte, P. (2018). Passive monitoring of a sea dike dur-  
581           ing a tidal cycle using sea waves as a seismic noise source. *Geophysical Journal*  
582           *International*, 214(2), 1364–1378.
- 583 Kamei, R., & Lumley, D. (2017). Full waveform inversion of repeating seismic events  
584           to estimate time-lapse velocity changes. *Geophysical Journal International*,  
585           209(2), 1239–1264.
- 586 Kennett, B., Stipčević, J., & Gorbatov, A. (2015). Spiral-arm seismic arrays. *Bul-*  
587           *letin of the Seismological Society of America*, 105(4), 2109–2116.
- 588 Kramer, R., Lu, Y., & Bokelmann, G. (2023). Interaction of air pressure and  
589           groundwater as main cause of sub-daily relative seismic velocity changes. *Geo-*  
590           *physical Research Letters*, 50(7), e2022GL101298.
- 591 Krevor, S., De Coninck, H., Gasda, S. E., Ghaleigh, N. S., de Gooyert, V., Ha-  
592           jibeygi, H., ... Swennenhuis, F. (2023). Subsurface carbon dioxide and  
593           hydrogen storage for a sustainable energy future. *Nature Reviews Earth &*  
594           *Environment*, 4(2), 102–118.
- 595 Larose, E., Margerin, L., Derode, A., van Tiggelen, B., Campillo, M., Shapiro, N.,  
596           ... Tanter, M. (2006). Correlation of random wavefields: An interdisciplinary  
597           review. *Geophysics*, 71(4), SI11–SI21.
- 598 Lecocq, T., Caudron, C., & Brenguier, F. (2014). MSNoise, a python package for  
599           monitoring seismic velocity changes using ambient seismic noise. *Seismological*  
600           *Research Letters*, 85(3), 715–726.
- 601 Li, J., Feng, Z., & Schuster, G. (2017). Wave-equation dispersion inversion. *Geophys-*  
602           *ical Journal International*, 208(3), 1567–1578.
- 603 Lindsey, N. J., Dawe, T. C., & Ajo-Franklin, J. B. (2019). Illuminating seafloor  
604           faults and ocean dynamics with dark fiber distributed acoustic sensing. *Sci-*  
605           *ence*, 366(6469), 1103–1107.
- 606 Longuet-Higgins, M. S. (1950). A theory of the origin of microseisms. *Philosophi-*  
607           *cal Transactions of the Royal Society of London. Series A, Mathematical and*  
608           *Physical Sciences*, 243(857), 1–35.
- 609 Lumley, D. (2001). Time-lapse seismic reservoir monitoring. *Geophysics*, 66(1), 50–  
610           53.

- 611 Lumley, D. (2010). 4D seismic monitoring of CO<sub>2</sub> sequestration. *The Leading Edge*,  
612 *29*(2), 150–155.
- 613 Mao, S., Campillo, M., van Der Hilst, R. D., Brenguier, F., Stehly, L., & Hillers,  
614 G. (2019). High temporal resolution monitoring of small variations in crustal  
615 strain by dense seismic arrays. *Geophysical Research Letters*, *46*(1), 128–137.
- 616 Mao, S., Ellsworth, W. L., & Beroza, G. C. (2023). Adaptive coda-wave imag-  
617 ing with voronoi tessellation. *Journal of Geophysical Research: Solid Earth*,  
618 *128*(8), e2023JB026592.
- 619 Mao, S., Lecointre, A., van der Hilst, R. D., & Campillo, M. (2022). Space-time  
620 monitoring of groundwater fluctuations with passive seismic interferometry.  
621 *Nature communications*, *13*(1), 4643.
- 622 Margerin, L., Planès, T., Mayor, J., & Calvet, M. (2016). Sensitivity kernels for  
623 coda-wave interferometry and scattering tomography: theory and numerical  
624 evaluation in two-dimensional anisotropically scattering media. *Geophysical  
625 Journal International*, *204*(1), 650–666.
- 626 Minato, S., Tsuji, T., Ohmi, S., & Matsuoka, T. (2012). Monitoring seismic velocity  
627 change caused by the 2011 Tohoku-oki earthquake using ambient noise records.  
628 *Geophysical Research Letters*, *39*(9).
- 629 Mordret, A., Courbis, R., Brenguier, F., Chmiel, M., Garambois, S., Mao, S., ...  
630 others (2020). Noise-based ballistic wave passive seismic monitoring—part 2:  
631 surface waves. *Geophysical Journal International*, *221*(1), 692–705.
- 632 Mordret, A., Rivet, D., Landès, M., & Shapiro, N. M. (2015). Three-dimensional  
633 shear velocity anisotropic model of Piton de la Fournaise Volcano (la réunion  
634 island) from ambient seismic noise. *Journal of Geophysical Research: Solid  
635 Earth*, *120*(1), 406–427.
- 636 Mordret, A., Shapiro, N. M., & Singh, S. (2014). Seismic noise-based time-lapse  
637 monitoring of the Valhall overburden. *Geophysical Research Letters*, *41*(14),  
638 4945–4952.
- 639 Nakata, N., Boué, P., Brenguier, F., Roux, P., Ferrazzini, V., & Campillo, M. (2016).  
640 Body and surface wave reconstruction from seismic noise correlations between  
641 arrays at Piton de la Fournaise volcano. *Geophysical Research Letters*, *43*(3),  
642 1047–1054.
- 643 Nishida, K. (2013). Earth’s background free oscillations. *Annual Review of Earth  
644 and Planetary Sciences*, *41*, 719–740.
- 645 Oakley, D. O., Forsythe, B., Gu, X., Nyblade, A. A., & Brantley, S. L. (2021). Seis-  
646 mic ambient noise analyses reveal changing temperature and water signals  
647 to 10s of meters depth in the critical zone. *Journal of Geophysical Research:  
648 Earth Surface*, *126*(2), e2020JF005823.
- 649 Obermann, A., Kraft, T., Larose, E., & Wiemer, S. (2015). Potential of ambient  
650 seismic noise techniques to monitor the St. Gallen geothermal site (Switzer-  
651 land). *Journal of Geophysical Research: Solid Earth*, *120*(6), 4301–4316.
- 652 Obermann, A., Planès, T., Larose, E., Sens-Schönfelder, C., & Campillo, M. (2013).  
653 Depth sensitivity of seismic coda waves to velocity perturbations in an elastic  
654 heterogeneous medium. *Geophysical Journal International*, *194*(1), 372–382.
- 655 Obermann, A., Schimmel, M., Weemstra, C., Verdel, A., & Jousset, P. (2013). Imag-  
656 ing preruptive and coeruptive structural and mechanical changes of a volcano  
657 with ambient seismic noise. *Journal of Geophysical Research: Solid Earth*,  
658 *118*(12), 6285–6294.
- 659 Pacheco, C., & Snieder, R. (2005). Time-lapse travel time change of multiply  
660 scattered acoustic waves. *The Journal of the Acoustical Society of America*,  
661 *118*(3), 1300–1310.
- 662 Pasqualini, D., Heitmann, K., TenCate, J. A., Habib, S., Higdon, D., & John-  
663 son, P. A. (2007). Nonequilibrium and nonlinear dynamics in Berea and  
664 Fontainebleau sandstones: Low-strain regime. *Journal of Geophysical Re-  
665 search: Solid Earth*, *112*(B1).

- 666 Planès, T., Rittgers, J. B., Mooney, M. A., Kanning, W., & Draganov, D. (2017).  
667 Monitoring the tidal response of a sea levee with ambient seismic noise. *Journal of Applied Geophysics*, *138*, 255–263.
- 668  
669 Poupinet, G., Ellsworth, W., & Frechet, J. (1984). Monitoring velocity variations  
670 in the crust using earthquake doublets: An application to the Calaveras Fault,  
671 California. *Journal of Geophysical Research: Solid Earth*, *89*(B7), 5719–5731.
- 672 Rentsch, S., Thompson, J., Adams, R., Moore, D., & Raborn, R. (2023). 100 Ocean  
673 Bottom Nodes with their CSAC clock drift analysed for 91 days: three controlled  
674 experiments. In *84th eage annual conference & exhibition* (Vol. 2023,  
675 pp. 1–5).
- 676 Richter, T., Sens-Schönfelder, C., Kind, R., & Asch, G. (2014). Comprehensive  
677 observation and modeling of earthquake and temperature-related seismic velocity  
678 changes in northern Chile with passive image interferometry. *Journal of Geophysical Research: Solid Earth*, *119*(6), 4747–4765.
- 679  
680 Ringrose, P. S., Furre, A.-K., Gilfillan, S. M., Krevor, S., Landrø, M., Leslie, R., . . .  
681 Zahid, A. (2021). Storage of carbon dioxide in saline aquifers: Physicochemical  
682 processes, key constraints, and scale-up potential. *Annual Review of Chemical and Biomolecular Engineering*, *12*, 471–494.
- 683  
684 Rodríguez Tribaldos, V., & Ajo-Franklin, J. B. (2021). Aquifer monitoring using  
685 ambient seismic noise recorded with distributed acoustic sensing DAS deployed  
686 on dark fiber. *Journal of Geophysical Research: Solid Earth*, *126*(4),  
687 e2020JB021004.
- 688 Roux, P., Sabra, K. G., Gerstoft, P., Kuperman, W., & Fehler, M. C. (2005). P-  
689 waves from cross-correlation of seismic noise. *Geophysical Research Letters*,  
690 *32*(19).
- 691 Sánchez-Pastor, P., Obermann, A., & Schimmel, M. (2018). Detecting and locating  
692 precursory signals during the 2011 El Hierro, Canary islands, submarine  
693 eruption. *Geophysical Research Letters*, *45*(19), 10–288.
- 694 Sánchez-Pastor, P., Obermann, A., Schimmel, M., Weemstra, C., Verdel, A., & Jousset,  
695 P. (2019). Short-and long-term variations in the reykjanes geothermal  
696 reservoir from seismic noise interferometry. *Geophysical Research Letters*,  
697 *46*(11), 5788–5798.
- 698 Saygin, E., Cummins, P. R., & Lumley, D. (2017). Retrieval of the P wave reflectivity  
699 response from autocorrelation of seismic noise: Jakarta Basin, Indonesia.  
700 *Geophysical Research Letters*, *44*(2), 792–799.
- 701 Saygin, E., & Kennett, B. (2012). Crustal structure of Australia from ambient  
702 seismic noise tomography. *Journal of Geophysical Research: Solid Earth*,  
703 *117*(B1).
- 704 Schimmel, M., Stutzmann, E., & Gallart, J. (2011). Using instantaneous phase  
705 coherence for signal extraction from ambient noise data at a local to a global  
706 scale. *Geophysical Journal International*, *184*(1), 494–506.
- 707 Sens-Schönfelder, C., & Eulendorf, T. (2019). Probing the in situ elastic nonlinearity  
708 of rocks with earth tides and seismic noise. *Physical review letters*, *122*(13),  
709 138501.
- 710 Sens-Schönfelder, C., & Wegler, U. (2006). Passive image interferometry and seasonal  
711 variations of seismic velocities at Merapi Volcano, Indonesia. *Geophysical research letters*, *33*(21).
- 712  
713 Shapiro, N. M., & Campillo, M. (2004). Emergence of broadband Rayleigh waves  
714 from correlations of the ambient seismic noise. *Geophysical Research Letters*,  
715 *31*(7).
- 716 Shen, X. (2010). Near-surface velocity estimation by weighted early-arrival waveform  
717 inversion. In *2010 seg annual meeting*.
- 718 Shipp, R. M., & Singh, S. C. (2002). Two-dimensional full wavefield inversion of  
719 wide-aperture marine seismic streamer data. *Geophysical Journal International*, *151*(2), 325–344.
- 720

- 721 Snieder, R., Grêt, A., Douma, H., & Scales, J. (2002). Coda wave interferometry  
722 for estimating nonlinear behavior in seismic velocity. *Science*, *295*(5563),  
723 2253–2255.
- 724 Stehly, L., Campillo, M., & Shapiro, N. (2006). A study of the seismic noise from  
725 its long-range correlation properties. *Journal of Geophysical Research: Solid  
726 Earth*, *111*(B10).
- 727 Takano, T., Brenguier, F., Campillo, M., Peltier, A., & Nishimura, T. (2020). Noise-  
728 based passive ballistic wave seismic monitoring on an active volcano. *Geophysical  
729 Journal International*, *220*(1), 501–507.
- 730 Takano, T., & Nishida, K. (2023). Tidal response of seismic wave velocity at shallow  
731 crust in Japan. *Geophysical Research Letters*, *50*(9), e2023GL103011.
- 732 Takano, T., Nishimura, T., Nakahara, H., Ohta, Y., & Tanaka, S. (2014). Seismic  
733 velocity changes caused by the Earth tide: Ambient noise correlation analyses  
734 of small-array data. *Geophysical Research Letters*, *41*(17), 6131–6136.
- 735 Takano, T., Nishimura, T., Nakahara, H., Ueda, H., & Fujita, E. (2019). Sensitivity  
736 of seismic velocity changes to the tidal strain at different lapse times: data  
737 analyses of a small seismic array at Izu-Oshima volcano. *Journal of Geophysical  
738 Research: Solid Earth*, *124*(3), 3011–3023.
- 739 Tarantola, A. (1984). Inversion of seismic reflection data in the acoustic approxima-  
740 tion. *Geophysics*, *49*(8), 1259–1266.
- 741 Tonegawa, T., Takagi, R., Sawazaki, K., & Shiomi, K. (2023). Short-term and  
742 long-term variations in seismic velocity at shallow depths of the overriding  
743 plate west of the Japan trench. *Journal of Geophysical Research: Solid Earth*,  
744 *128*(1), e2022JB025262.
- 745 Tromp, J., Tape, C., & Liu, Q. (2005). Seismic tomography, adjoint methods, time  
746 reversal and banana-doughnut kernels. *Geophysical Journal International*,  
747 *160*(1), 195–216.
- 748 Viens, L., Denolle, M. A., Hirata, N., & Nakagawa, S. (2018). Complex near-surface  
749 rheology inferred from the response of greater Tokyo to strong ground mo-  
750 tions. *Journal of Geophysical Research: Solid Earth*, *123*(7), 5710–5729.
- 751 Virieux, J. (1986). P-SV wave propagation in heterogeneous media: Velocity-stress  
752 finite-difference method. *Geophysics*, *51*(4), 889–901.
- 753 Weaver, R., Froment, B., & Campillo, M. (2009). On the correlation of non-  
754 isotropically distributed ballistic scalar diffuse waves. *The Journal of the  
755 Acoustical Society of America*, *126*(4), 1817–1826.
- 756 Wegler, U., Lühr, B.-G., Snieder, R., & Ratdomopurbo, A. (2006). Increase of  
757 shear wave velocity before the 1998 eruption of Merapi volcano (Indonesia).  
758 *Geophysical Research Letters*, *33*(9).
- 759 Yamamura, K., Sano, O., Utada, H., Takei, Y., Nakao, S., & Fukao, Y. (2003).  
760 Long-term observation of in situ seismic velocity and attenuation. *Journal of  
761 Geophysical Research: Solid Earth*, *108*(B6).
- 762 Yang, D., Liu, F., Morton, S., Malcolm, A., & Fehler, M. (2016). Time-lapse full-  
763 waveform inversion with ocean-bottom-cable data: Application on Valhall field.  
764 *Geophysics*, *81*(4), R225–R235.
- 765 Yates, A., Savage, M., Jolly, A., Caudron, C., & Hamling, I. (2019). Volcanic, coseis-  
766 mic, and seasonal changes detected at White Island (Whakaari) volcano, New  
767 Zealand, using seismic ambient noise. *Geophysical Research Letters*, *46*(1),  
768 99–108.
- 769 Yuan, Y. O., Simons, F. J., & Tromp, J. (2016). Double-difference adjoint seismic  
770 tomography. *Geophysical Journal International*, *206*(3), 1599–1618.
- 771 Zhang, S., Luo, B., Ben-Zion, Y., Lumley, D. E., & Zhu, H. (2023). Monitoring ter-  
772 restrial water storage, drought and seasonal changes in central Oklahoma with  
773 ambient seismic noise. *Geophysical Research Letters*, *50*(17), e2023GL103419.
- 774 Zhang, Z., & Huang, L. (2013). Double-difference elastic-waveform inversion with  
775 prior information for time-lapse monitoring. *Geophysics*, *78*(6), R259–R273.

- 776 Zheng, Y., Barton, P., & Singh, S. (2011). Strategies for elastic full waveform in-  
777 version of time-lapse ocean bottom cable (OBC) seismic data. In *Seg technical*  
778 *program expanded abstracts 2011* (pp. 4195–4200). Society of Exploration Geo-  
779 physicists.
- 780 Zhou, W., & Lumley, D. (2021). Nonrepeatability effects on time-lapse 4D seismic  
781 full-waveform inversion for ocean-bottom node data. *Geophysics*, *86*(4), R547–  
782 R561.
- 783 Zhu, T., Ajo-Franklin, J., Daley, T. M., & Marone, C. (2019). Dynamics of geologic  
784 CO<sub>2</sub> storage and plume motion revealed by seismic coda waves. *Proceedings of*  
785 *the National Academy of Sciences*, *116*(7), 2464–2469.
- 786 Zinszner, B., Johnson, P. A., & Rasolofosaon, P. N. (1997). Influence of change in  
787 physical state on elastic nonlinear response in rock: Significance of effective  
788 pressure and water saturation. *Journal of Geophysical Research: Solid Earth*,  
789 *102*(B4), 8105–8120.